




# Fabrication of Integrated Lensless Cameras via UV-Imprint Lithography

Yujin Lee , Hyesuk Chae, Kyung Chul Lee, Nakkyu Baek, Taeyoung Kim , Jaewoo Jung, and Seung Ah Lee , *Member, IEEE*

**Abstract**—We report on the construction of a lensless camera with a phase-modulating mask layer integrated directly on an image sensor using the UV-imprint lithography method. By replicating the master phase mask’s surface structure directly on the image sensor, our method further simplifies the fabrication of lensless cameras and delivers a rigid and durable device with a small form factor. Our prototype device has an open-faced design without any apertures and generates high-quality photographic reconstructions with high light collection efficiency. We analyze the performance of our prototype device and demonstrate various imaging applications, including the digital refocusing capabilities.

**Index Terms**—Lensless imaging, fabrication method, ultra-thin camera, low-cost imaging device, computational imaging, lithography.

## I. INTRODUCTION

CAMERAS are becoming an essential sensing and recording modality in various devices, including smartphones, wearables, the Internet of Things (IoT), and medical devices. With this increasing demand, there has been much effort to further miniaturize the optics of the cameras at a low manufacturing cost [1]–[4]. Wafer-level manufacturing and packaging processes for the image sensors and the lens elements have been developed for miniature camera modules [5], [6]; however, there are physical limits in reducing the thickness of conventional lenses, especially with the increasing pixel resolution of image sensors. Other approaches, such as compound-eye cameras using lenslet arrays [7] or thin metalenses with precisely-designed and fabricated nanostructures [8] have also been demonstrated, usually with trade-offs in image quality or the manufacturing cost.

As an alternative approach, lensless cameras using light-modulating masks have been recently proposed and demonstrated [9]–[27]. Instead of using lenses to form images on the image sensor, lensless cameras use amplitude- or phase

masks with known light-modulating properties and rely on computational algorithms to reconstruct the scene from the sensor’s measurement, achieving ultra-thin, light, and scalable form-factor at a low cost. Lensless cameras using coded-aperture-based amplitude masks can be fabricated and integrated with the image sensor in wafer-level processes with minimal device thickness ( $<500 \mu\text{m}$ ) [20], [23]. However, phase mask-based lensless cameras using weak diffusers [28] or designed diffractive elements [19] have higher light collection efficiency, less computational complexity in image reconstruction, better image quality, and multiplexing capabilities. With these advantages, a wide range of lensless imaging applications have been recently reported, including photography (photorealistic, video from stills, hyperspectral) [18], [24], microscopy [13], [21], [25], light-field imaging [26], 3D imaging [19], and endoscopy [14], [27].

In phase mask-based lensless cameras, the mask placed in front of the image sensor determines the transfer function of the imaging system [28]. The microscopic structures in the phase masks create a two-dimensional point-spread function (PSF) which is shift-invariant, and the imaging system’s forward model can be modeled as a convolution between the scene and the 2D PSF (Fig. 1(a)). With known PSF, the blurry raw measurement from the image sensor (Fig. 1(c)) can be computationally deconvolved to reconstruct the image of the scene. Thus, in assembling a lensless camera, it is essential to place the phase mask at the proper distance from the image sensor such that the mask creates sharp and high-contrast PSF, which is crucial for the reconstruction of high-quality images. In most previous demonstrations, a separately fabricated phase mask film (weak diffusers [18], [26], [28] or diffractive phase masks [14], [19]) was placed on a spacer and manually assembled with the image sensor. However, for mass production of these lensless cameras, this method is not exceptionally reliable, and also the structure itself is mechanically unstable. Any misalignment in the phase mask or the structural changes in the phase mask may lead to the deviation of the camera’s forward model from the designed or calibrated PSF and degrade the final image quality.

In this paper, we propose a reliable and straightforward fabrication method for phase mask-based lensless cameras, where the microscopic surface pattern of the phase mask is imprinted directly on top of a working CMOS image sensor. We use the UV-imprinting method with a replica mold of a phase mask to create a layer of transparent resin with phase-modulating properties on the image sensor, removing the need to align and

Manuscript received January 17, 2022; revised February 27, 2022; accepted March 1, 2022. Date of publication March 8, 2022; date of current version March 31, 2022. This work was supported by the National Research Foundation of Korea Grant 2021R1C1C101290011 funded by the Korean government (MSIT). (Yujin Lee and Hyesuk Chae contributed equally to this work.) (Corresponding author: Seung Ah Lee.)

The authors are with the School of Electrical and Electronic Engineering, Yonsei University, Seoul 03722, Republic of Korea (e-mail: dbwls3284@yonsei.ac.kr; chs111@yonsei.ac.kr; lkc724@yonsei.ac.kr; whitenk@yonsei.ac.kr; falcon@yonsei.ac.kr; lukael.jung@yonsei.ac.kr; seungahlee@yonsei.ac.kr).

Digital Object Identifier 10.1109/JPHOT.2022.3157373

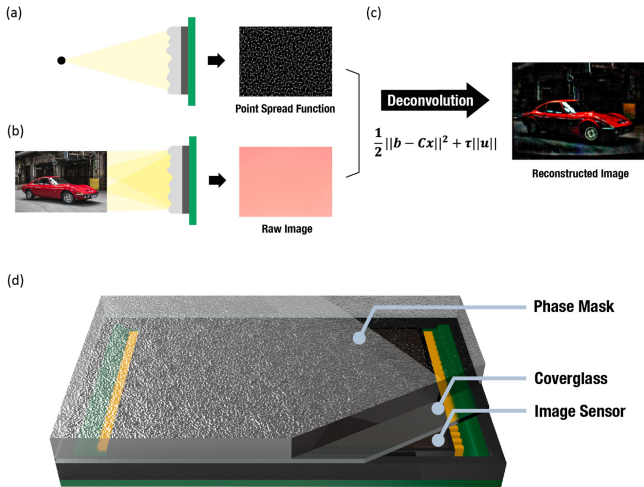


Fig. 1. (a) Formation of 2D point spread function (PSF) in a phase-mask-based lensless camera. (b) Imaging the scene with the lensless camera. The image sensor's measurement corresponds to the convolution between the scene and the 2D PSF. (c) Reconstruction of the scene using computational deconvolution methods. (d) Structure of our lensless camera with phase mask layer fabricated directly on top of the image sensor using the UV-imprinting method.

assemble multiple components. The process is simple, low-cost, highly repeatable, and scalable, and the final device is robust and stable, demonstrating the feasibility of the integrated fabrication process for the production of lensless cameras at scale. Furthermore, we show that our lensless camera achieves a very compact form factor yet produces high-quality images without any aperture on the phase mask. In the following sections, we describe the design and fabrication methods in detail and analyze the imaging performance of our device.

## II. DESIGN AND FABRICATION

A lensless camera is composed of an image sensor and a phase mask held in place at a focal length away from the sensor plane [19], [28]. Typically, a spacer of predesigned thickness is used to guarantee this spacing, and a finite-sized aperture is placed to limit the 2D PSF of the camera to fit the active area of the image sensor. Commercially available weak diffuser films have been widely used as phase masks [18], [26], [28], which has smooth and randomized surface profiles that create pseudo-random caustic PSF patterns on the image sensor. Surface curvatures on the diffuser determine the PSF's density and sharpness, and the diffuser's focal length, which is defined as the distance to the plane where the sharpest PSF is formed. These weak diffuser films are usually fabricated in lithographic methods [29], [30] or chemical etching processes [31], which are not suited for generating predesigned structures nor easy to integrate directly onto the image sensor. Recently, methods for designing phase mask structures for specific pre-determined 2D PSF patterns and fabricating the mask structure via two-photon nano 3D printing have been reported [19]. Unlike the diffuser-based lensless cameras, this method allows one to precisely choose the PSF and the resulting specifications of the lensless camera, thus enabling a more versatile design of lensless cameras for specific applications. Nevertheless, fabrication of the phase mask using

two-photon lithography can be too costly for the mass production of the device.

We used a UV-imprinting-based replication method to integrate phase masks with image sensors in a low-cost and high-throughput manner. Once the master phase mask for the lensless camera is predesigned and fabricated, the same mask can be replicated directly on the CMOS image sensor to create an on-chip lensless camera. With the initial phase mask as the master, we first perform soft-lithography to create a mold and then perform UV imprint to create a replica phase mask on the image sensor. The master phase mask can be any mask with surface profiles, including diffusers, lenslet arrays, or designed diffractive masks. In our experiments, we used a commercial diffuser used in many lensless camera literatures as a master phase mask and fabricated a layer of UV-curable transparent resin with replicated surface profiles that work as a phase-modulating layer for lensless imaging.

In phase mask-based lensless cameras, the distance between the mask and the sensor needs to precisely match the distance for which the phase mask is designed or the distance at which the mask creates a sharp and high-contrast PSF. The phase-modulating property of the mask is determined by the optical path length differences that the mask generates; thus, the refractive index of the material, as well as the height profile of the mask, needs to be considered. In making the replicated mask layer on the sensor, we first need to determine the thickness of the layer in consideration of the refractive index of the replica, which will create a sharp PSF on the sensor plane.

To compute the optimal thickness of the replicated mask layer, we first built a simple ray-tracing model using ray transfer matrix analysis. We modeled the surface profile of the master phase mask as the randomly distributed microlens array with an average radius of curvature that defines the focal length of the camera. Since this surface curvature is unknown, we first measured the distance from the image sensor at which the master phase mask creates the sharpest PSF. Then we obtained the accurate radius of curvature of the phase mask using the ray transfer matrix model as shown in Fig. 2(a). With the phase mask film with thickness  $t_p$  placed at distance  $d_p$  in front of the image sensor with the cover glass, the ray transfer matrix equation can be written as below.

$$\begin{bmatrix} y' \\ \theta' \end{bmatrix} = \begin{bmatrix} 1 & d_g \\ 0 & 1 \end{bmatrix} \begin{bmatrix} 1 & 0 \\ 0 & \frac{n_g}{n_0} \end{bmatrix} \begin{bmatrix} 1 & t_g \\ 0 & 1 \end{bmatrix} \begin{bmatrix} 1 & 0 \\ 0 & \frac{n_0}{n_g} \end{bmatrix} \begin{bmatrix} 1 & d_p \\ 0 & 1 \end{bmatrix} \\ \times \begin{bmatrix} 1 & 0 \\ 0 & \frac{n_p}{n_0} \end{bmatrix} \begin{bmatrix} 1 & t_p \\ 0 & 1 \end{bmatrix} \begin{bmatrix} 1 & 0 \\ \frac{n_0 - n_p}{R n_p} & \frac{n_0}{n_p} \end{bmatrix} \begin{bmatrix} y \\ \theta \end{bmatrix} \quad (1)$$

Here,  $y$  and  $\theta$  are the position and angle of the incident ray, and  $y'$  and  $\theta'$  are the position and angle at the sensor plane.  $n_0$ ,  $n_p$ ,  $n_g$  are the refractive indices of air ( $n_0 = 1$ ), phase mask (poly-carbonate,  $n_p = 1.59$ ), and the cover glass ( $n_g = 1.52$ ), respectively.  $t_g$  is the thickness of the covered glass, and  $d_g$  is the distance between the covered glass and the sensor plane, which need to be measured for each image sensor. We measured

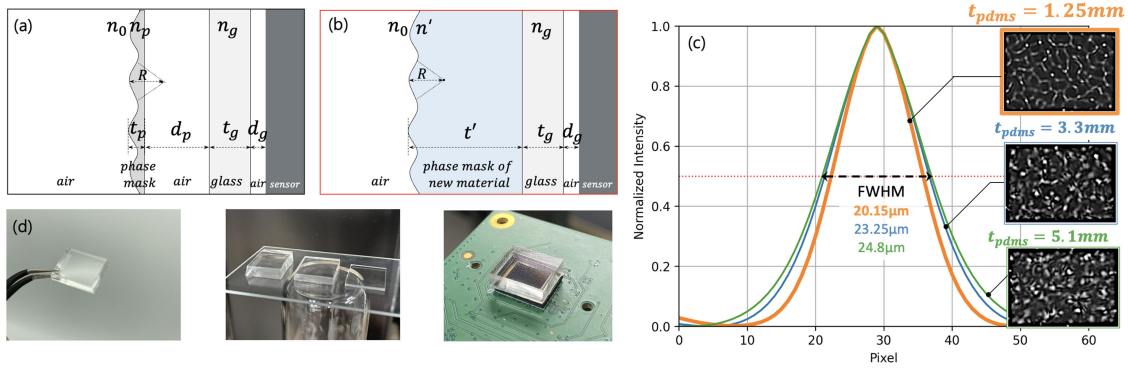


Fig. 2. Design and characterization of imprinted phase mask layer on the lensless camera. (a) Model of the conventional lensless camera with space between the master diffuser film and the image sensor for ray transfer matrix analysis. (b) Integrated lensless camera model for ray transfer matrix analysis for designing the film thickness  $t'$ . (c) Line trace of the auto-correlations of the PDMS-based diffuser films with different thicknesses. (d) PDMS diffuser films for used in (c) for verification of the ray transfer matrix model.

the value of  $d_p$  that makes the sharpest PSF with minimum full-width at half maximum (FWHM) to determine  $R$ , the radius of curvature. The transfer matrices in (1) can be simplified into a single matrix as below,

$$\begin{bmatrix} y' \\ \theta' \end{bmatrix} = \begin{bmatrix} N_{11} & N_{12} \\ N_{21} & N_{22} \end{bmatrix} \begin{bmatrix} y \\ \theta \end{bmatrix} \quad (2)$$

For input parallel rays to converge at one point on the image sensor plane, the value of  $N_{11}$  has to be 0. With this condition, we can derive the following equation for  $R$ .

$$R = \frac{n_p - n_0}{n_p} \left[ t_p + t_g + \frac{n_p}{n_0} (d_g + d_p) \right] \quad (3)$$

Now we switch the material to form replicated diffuser layer with the same surface curvature  $R$  but with refractive index  $n'$  and the new thickness  $t'$  that comes in contact with the cover glass of the image sensor, as shown in Fig. 2(b). The ray transfer matrix equation now becomes,

$$\begin{bmatrix} y' \\ \theta' \end{bmatrix} = \begin{bmatrix} 1 & d_g \\ 0 & 1 \end{bmatrix} \begin{bmatrix} 1 & 0 \\ 0 & \frac{n_g}{n_0} \end{bmatrix} \begin{bmatrix} 1 & t_g \\ 0 & 1 \end{bmatrix} \begin{bmatrix} 1 & 0 \\ 0 & \frac{n'}{n_g} \end{bmatrix} \begin{bmatrix} 1 & t' \\ 0 & 1 \end{bmatrix} \times \begin{bmatrix} 1 & 0 \\ \frac{n_0 - n'}{Rn'} & \frac{n_0}{n'} \end{bmatrix} \begin{bmatrix} y \\ \theta \end{bmatrix} \quad (4)$$

With the same focusing condition, the thickness of the new replicated diffuser layer can be written as

$$t' = \frac{Rn'}{n' - n_0} - \frac{n'}{n_g} \left( t_g + d_g \frac{n_g}{n_0} \right) \quad (5)$$

As a preliminary experiment to verify our ray transfer matrix analysis, we first choose PDMS as the on-sensor diffuser material due to the ease of casting and thickness control. For the master phase mask, we used a commercial light shaping diffuser (Luminit, L1P1-12, 1° FWHM). For integration and focal-length measurement, we used a Raspberry Pi High-Quality Camera with a Sony IMX477 image sensor. The  $t_g$  and  $d_g$  values of the image sensor were measured prior to the experiment to be 0.49 and 0.235 mm, respectively. The  $d_p$  value for the master diffuser

measured from the PSF autocorrelation was  $0.4 \pm 0.2$  mm, which results in  $R$  of  $\sim 0.67$  mm. Considering the average focal length of the mask ( $\sim 1$  mm) and the average pattern density calculated from the density of the PSFs, the average numerical aperture of each lenslet is  $\sim 0.035$ , with an estimated depth of focus of  $\sim 0.41$  mm. In our experiments, the PSFs of the master diffuser had the same sharpness under  $d_p$  between 0.2 to 0.6 mm, which corresponds to the estimated depth of focus of the diffuser. Note that within the  $d_p$  range, the overall sharpness of the 2D PSF is equally high, thus will provide good image quality for the lensless imaging. However, the actual PSFs at each  $t'$  appear slightly different because of the different focal lengths of the local features on the mask.

With the computed value of  $R$ , we calculated for the optimal thickness  $t'$  of a PDMS replica of the diffuser. With the refractive index of  $n' = 1.43$ , the calculated  $t'$  was  $1.44 \pm 0.41$  mm. For validation, we fabricated poly-dimethyl siloxane (PDMS) elastomer replicas with varying thicknesses and measured the resulting PSFs and their sharpnesses. Fig. 2(c, inset) shows the resulting PSF patterns for PDMS films with different thicknesses placed directly on the cover glass of the image sensor. The FWHM of the autocorrelation of the 2D PSF of PDMS diffusers confirmed that film with thickness  $t' = 1.25$  mm has the sharpest PSFs among the films we have made, with FWHM of 20.15  $\mu\text{m}$ .

With the same model, we computed the optimal thickness of the replica mask layer fabricated with UV-curable resin. In the actual fabrication of the device, we used polyurethane acrylate (PUA) 311 (MINS 311-RM, Minuta tech, Korea) resin for the UV-imprinting process. PUA311 has high optical transmittance in the visible wavelengths ( $>90\%$  at 1-mm thickness) and good mechanical properties to make a solid diffuser layer. It has refractive index of  $n' = 1.47$ , resulting in the optimal thickness of  $t' = 1.28 \pm 0.37$  mm. The calculated ranges of  $t'$  for both PDMS and PUA311 masks have a relatively wide range due to the effect of the master diffuser's focal characteristics, and the PSFs within this range are expected to show same sharpness as seen in the master diffuser. However, it is worth noting that because the actual PSF pattern may vary within this range, if multiple cameras with the same 2D PSF need to be fabricated,  $t'$  needs to be controlled with high precision. With these design

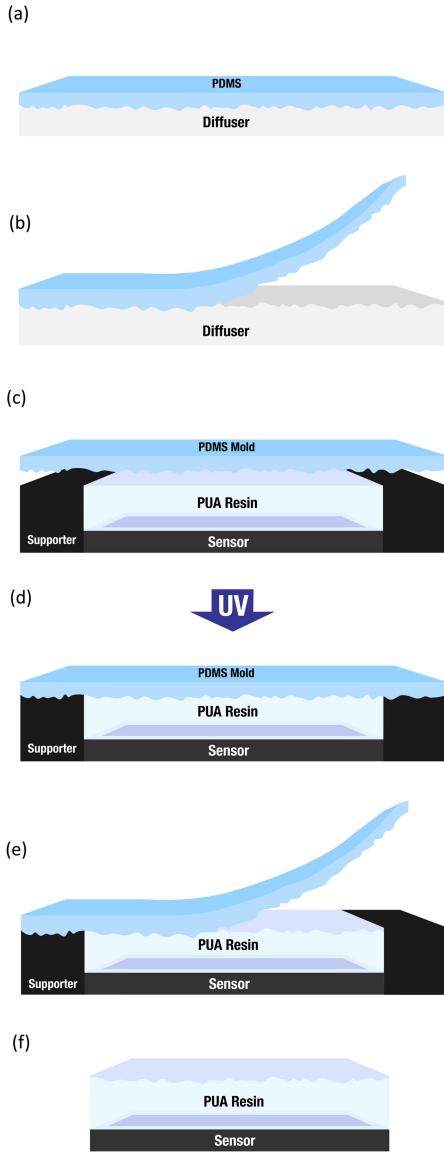


Fig. 3. UV-imprint lithography process for lensless camera fabrication. (a)–(b) Soft-lithography for PDMS mold against the master phase mask (diffuser film). (c) PUA resin is applied on the image sensor and the PDMS mold is placed on the supporter and the PUA resin. (d) The resin is exposed under UV light for curing. (e)–(f) Detaching the PDMS mask forms the integrated lensless camera.

parameters, we fabricated the replicated mask layer accordingly to create in-focus PSFs for our imaging applications.

For the fabrication of the on-chip lensless camera with a replicated mask layer directly imprinted on the working CMOS image sensor, we used the UV-imprinting process as illustrated in Fig. 3. First, we fabricate the mold via PDMS soft-lithography to be used with the UV-imprinting process to cast the exact replica of the master phase mask. We mix Sylgard 184 (Sewang Hitech) with the curing agent at a 6:1 ratio and pour it over the master diffuser. After degassing and baking in the oven at 80 Celsius for 1 h, the PDMS mold is detached for the imprinting process. Next, we attach a 3D-printed spacer around the image sensor to guarantee the designed thickness of the PUA layer ( $t' = 1.06$  mm) and to support the PDMS mold for

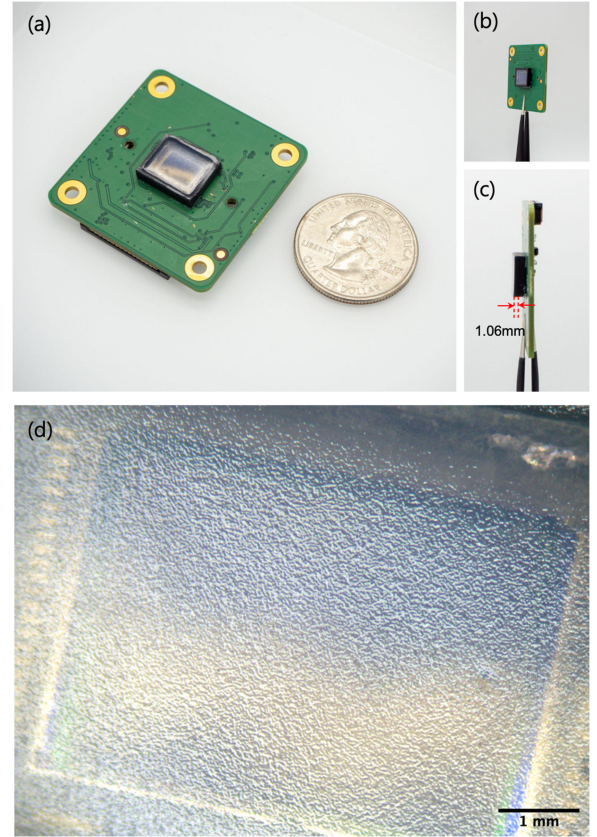


Fig. 4. (a)–(c) Photographs of our prototype lensless camera device. The thickness of the PUA phase mask layer is 1.06 mm. (d) Surface structures of the fabricated mask layer captured via a digital microscope.

UV-imprinting. After depositing a premeasured volume of the PUA resin on the image sensor and degassing to remove any air bubbles, the PDMS mold is placed on the supporter and the PUA resin, as depicted in Fig. 3(b). Then, the entire assembly is exposed under ultraviolet light (Fig. 3(c)) for 5 minutes. We use the UV chamber (Ahtech) with a 35 W UV lamp. Finally, the PDMS mold is taken off, and the surface of the cured PUA resin (Fig. 3(e)) follows an identical surface structure to the original diffuser.

### III. RESULT AND DISCUSSION

Our prototype lensless camera with an integrated phase mask layer is fabricated on a Raspberry Pi High-Quality Camera image sensor (IMX477,  $4056 \times 3040$  pixels, pixel size:  $1.55 \mu\text{m}$ ). Fig. 4 shows the photographs of the fabricated device. The size of the entire lensless camera module, including the image sensor and the 3D wall structure, is  $12.98 \times 11.15 \times 3$  mm, excluding the printed circuit board the sensor is soldered on. The 3D printed frame for casting PUA resin also functions as optically blocking the unwanted light entering the camera from the side. To simplify the manufacturing process, we did not place any aperture on the mask layer and opened the entire sensor plane, as shown in Fig. 4(d).

The 2D PSF of the fabricated lensless camera is shown in Fig. 5(a). The PSF is captured with a point-source illumination

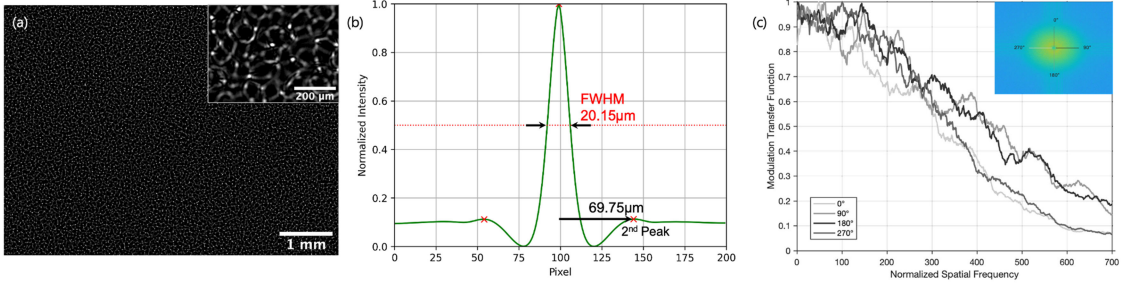


Fig. 5. (a) The PSF of the prototype camera (b) Line trace of the auto-correlation of the PSF (c) Modulation Transfer Function (MTF) of the prototype camera with Fourier magnitude spectrum of the PSF (inset).

using a white-LED with a 50-micron-pinhole placed at a working distance of 30 cm. Fig. 5(b) plots the normalized auto-correlation of 2D PSF with the FWHM of  $20.15 \mu\text{m}$ , which is identical to the sharpest FWHM measured with the PDMS-based diffuser in Fig. 2(c). Assuming that the line profile of the PSF pattern follows a Gaussian profile, the FWHM of the PSF line can be computed as  $14.25 \mu\text{m}$ . The image sensor used in our prototype has  $1.55 \mu\text{m}$ -pixels with a Bayer color filter array, so the line width of the PSF roughly corresponds to 4.6 effective pixels. The linewidth of the PSF pattern in our lensless camera is larger than the Airy-disc size of typical lenses due to the relatively low effective NA of the microscopic features on the diffuser. However, in lensless cameras, the image resolution is not solely dependent on the linewidth of the PSF pattern but also on the reconstruction algorithm, the complexity of the object, and the SNR of measurement [28], which we experimentally analyze in the next section of this paper.

From the 2D PSF, we can also obtain the density of the PSF. Since the PSF has a pseudo-random caustic pattern, we obtain the average density from the autocorrelation curve of the 2D PSF by measuring the distance between the first and the second peak, as shown in Fig. 5(b). With the average pitch of the PSF pattern of  $69.75 \mu\text{m}$ , equivalent to 45 pixels. The estimated average NA of each lenslet feature is around 0.035. With the fixed focal length of the lensless cameras, the PSF with lower density (more 0 values) and sharper linewidth with higher contrast ultimately give better image reconstruction under a finite bit-depth of the image sensor. However, the feature density and the NA are inversely proportional to each other. Thus there may be an optimal pattern density under a given focal length and the pixel size of the sensor, which needs to be further investigated for the design of the optimal phase masks for lensless cameras. Fig. 5(c) shows a modulation transfer function (MTF) of the camera obtained by the magnitude of the 2D Fourier transform of the PSF (inset). Line profiles of the Fourier spectrum over the direction of  $0^\circ$ ,  $90^\circ$ ,  $180^\circ$ ,  $270^\circ$  was plotted as a function of normalized spatial frequency, which confirms that the MTF curve in all directions is consistent.

Unlike the lensed cameras forming a point-to-point matching between the scene and the image sensor plane, lensless cameras disseminate all spatial information of the scene and create unidentifiable images on the sensor. Thus, computational image reconstruction must be accompanied. Under sufficient imaging conditions such as a finite field-of-view (FoV), a sufficient

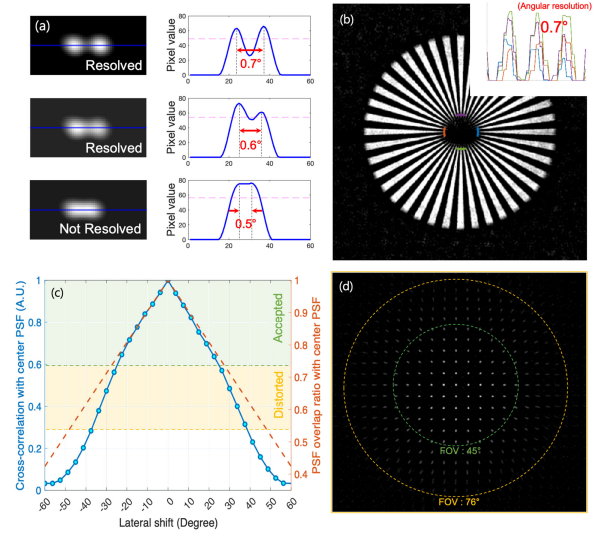


Fig. 6. Characterization of resolution and field of view (FoV) of the prototype device. (a) Reconstructed two-points resolution images showing the angular resolution limit of the camera. (b) Reconstructed images of a Siemens star target and the sampled line traces (inset). (c) Shift-variance of the PSFs measured via peak cross-correlation values of the PSFs at varying angle-of-views and the overlap ratio of the shifted PSFs. (d) FoV of the camera measured with a dotted grid (distance between dots: 2.3 mm, working distance : 300 mm).

distance from phase mask to sensor, and far-field approximation, the forward model for 2D imaging in lensless cameras can be approximated as a linear convolution between the scene and the 2D PSF of the camera [19], [28].

$$b = CMv \quad (6)$$

Here,  $v$  is a vectorized 2D intensity of the object scene,  $M$  is a matrix operator equivalent to the 2D convolution with the PSF kernel,  $C$  is the crop operator by the size of the image sensor, and  $b$  is the captured measurement.

To reconstruct the image, we used optimization-based deconvolution using alternating direction method of multipliers (ADMM) algorithm [32] that solves the following optimization problem with variable splitting.

$$\begin{aligned} & \text{minimize} \quad \frac{1}{2} \|b - Cx\|^2 + \tau \|u\|_1 \\ & \text{subject to} \quad x = Mv, u = \Psi v, w = v, w \geq 0 \end{aligned} \quad (7)$$

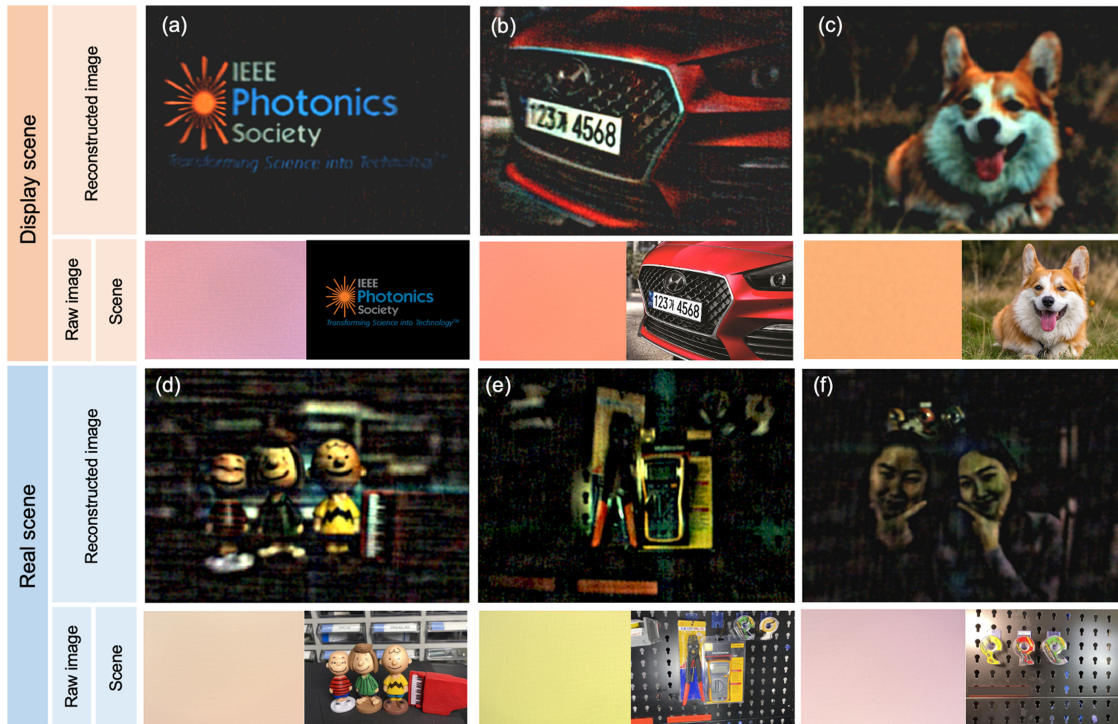


Fig. 7. Photography images of the display scenes (a)–(c) and real scenes (d)–(f) from the prototype device.

$\Psi$  is the gradient operator, and  $\tau$  is the weight on the total variation regularization term.

To evaluate the imaging performance of our camera, we experimentally measured the resolution and the FoV of our camera. In lensless cameras, the resolution of the reconstructed images is highly dependent on the scene itself [28], so there is no optimal way to fully describe the resolving power of the camera. Here, we chose to characterize the resolution limit using two experimental methods. First, the two-point resolution was measured by the 180 mm working distance at varying the separation of 2 LEDs working distances. As a result, the minimum resolvable angular resolution that meets the Rayleigh criterion was  $0.6^\circ$  (Fig. 6(a)). Secondly, we imaged a complex object, a Siemens star target, displayed on a screen (Fig. 6(b)). The reconstructed image revealed that the maximum angular resolution resolvable in all directions is  $0.73^\circ$  for the case of the Siemens target. We believe that the two-point resolution is the maximum resolution that the camera can achieve with any object.

To evaluate the FoV of our camera, we first measured the amount of shift-variance of the PSF pattern. We measured the PSF pattern with point source located at varying viewing angles from the camera and measured the cross-correlations between the center PSF and the laterally shifted PSFs. As shown in Fig. 6(c), the cross-correlation value decreases rapidly and completely loses correlation at the half-angle of  $50^\circ$ , indicating that the convolution-based forward model fails at large incident angles. We followed up this result with an imaging experiment using a target of a dotted grid pattern over a large angular FoV. Fig. 6(d) reveals that dots within  $45^\circ$  FoV are clearly captured, whereas those at FoV above  $45^\circ$  are aberrated with coma, field curvature, and vignetting. Above  $76^\circ$  FoV, the dots

are not reconstructed, indicating the maximum angular FoV of our camera. These angular regions correspond to the PSF cross-correlation value of above 0.6 to give acceptable image quality, between 0.6 and 0.3 to be distorted, and below 0.3 to be unresolved.

The limit in the angular FoV and the rapid drop in the cross-correlation can attribute to three factors; First, the pixels in the image sensor have a finite acceptance angle owing to the refractive index differences and the pixel geometry. At large incident angles, the light collection efficiency of the sensor drops significantly and creates significant vignetting in the reconstructed images, ultimately limiting the angular FoV of the camera. Secondly, since there is no aperture and the phase mask area is larger than the image sensor's active area, as the ray's incident angle changes, the shifted PSF pattern is partially cropped out of the sensor, and the new section of the PSF appears on the other side. As a result, the fraction of overlapping area between the center and the shifted PSFs decreases by 9.7% per every  $10^\circ$ , causing the correlation to drop with increasing incident angles gradually. Lastly, the PSF itself becomes aberrated at large incident angles. In the case of diffusers, typical monochromatic aberrations such as field curvature and coma can yield the shift-variance of the PSF patterns. The last two factors cause the camera's forward model to deviate from the convolution-based forward model, causing image quality degradations and unwanted artifacts in the backgrounds of the reconstructed images. The detrimental effect of the non-overlapping PSFs can be mitigated by putting a finite aperture on the image sensor or using a larger PSF stitched over a wider angular region. However, we observe that the reconstructed image quality of our camera is acceptable in the current form.

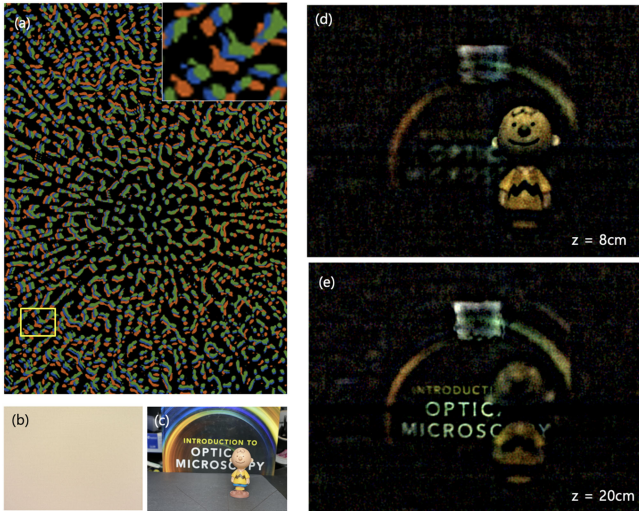


Fig. 8. Digital refocusing of the images. (a) The PSF magnification changing with the imaging depth. (Red :  $z = 3$  cm, Blue :  $z = 8$  cm, Green :  $z = 20$  cm, PSF image binarized for visualization). (b) The raw image. (c) Scene (d)-(e) Digitally-refocused images at 8 and 20 cm, respectively.

We performed 2D imaging with our prototype camera under various imaging conditions. Fig. 7(a)–(c) shows the raw and reconstructed lensless camera images captured with target images displayed on a screen. The camera was placed at a 30 cm working distance from the screen, and the target images were displayed at angular sizes of  $60^\circ$ ,  $50^\circ$ , and  $30^\circ$ . The raw images were captured with the exposure time of 40–70 ms, filling the 12-bit bit-depth of the pixels below the saturation level. Fig. 7(d)–(f) are the images that captured natural objects and scenes under working distances of 10, 50, and 60 cm, respectively. Under photography lighting conditions, exposure times of 9–15 ms were used.

Images are reconstructed with 500–1000 iterations of ADMM cycles with hand-tuned parameters. For images at different working distances, we used the PSF captured at the corresponding distance for reconstruction. Considering the sharpness of the PSFs and the measured resolution, we resized the PSF and the raw images by  $0.5 \times (2028 \times 1520)$  pixels for the reconstruction process. The elapsed time for reconstruction is up to 250 s for using NVIDIA RTX3090 with Intel Xeon GOLD 6242 CPU under Ubuntu 20.04. The reconstructed images well match the original scene and resolve fine details such as small letters and patterns on the scene. As predicted, vignetting and aberration exist at the outer regions of the images, such as the distortion of the letters on the bottom line of Fig. 7(a). The overall quality of images is comparable with other lensless imaging literature using optimization-based reconstruction methods. The reconstruction quality can be further improved by using deep-learning-based reconstruction that accounts for the imperfections in the forward model and includes image enhancement layers [33]–[36].

Lensless cameras allow digital refocusing and 3D imaging using depth-dependent PSFs. The PSF magnification changes depending on the working distance, as shown in Fig. 8(a). PSFs measured at short working distances have an enlarged pattern; For example, compared to the PSF at the working distance of 20 cm, PSF at 8 cm was enlarged by 0.36% and

3 cm 1.32%. Working distances above 30 cm did not show any noticeable changes in the PSF patterns with our camera. We imaged two objects at 8 cm (doll) and 20 cm (book) away from the camera. The images reconstructed with corresponding PSFs (Fig. 8(d)–(e)) show digitally refocused images of two objects alternatingly in focus. Due to the mismatch in the forward model, the object at a different distance appears blurry.

#### IV. CONCLUSION

We reported a simple fabrication method for a lensless camera where a phase-modulating layer of UV-curable resin is integrated directly on an image sensor. The UV-imprinting method allows replicating the master phase mask’s surface structure on the integrated lensless camera in a scalable manner. Our method removes the need to assemble separately fabricated phase masks and apertures and delivers a rigid and durable lensless camera with a small form factor. The prototype device has a total of 1.7 mm-thickness, including the image sensor, and produces photographic images over  $75^\circ$  FoV with the maximum estimated angular resolution of  $0.6^\circ$ . Without any aperture to block unwanted information, our prototype can still generate high-quality reconstructions comparable to other lensless cameras with small apertures while achieving very high light collection efficiency. We have analyzed the performance of our prototype device and showed example images of various scenes, including the digital refocusing capabilities.

Our method, currently in a proof-of-concept stage, can be further improved to produce lensless cameras at the wafer level to produce ultra-thin and low-cost imaging devices at scale. We demonstrated our method with an image sensor with a cover glass; nevertheless, the same process can be repeated directly on the active layer of the image sensor, which will make the design process more straightforward. Furthermore, the material and the design can be optimized to guarantee high fabrication yield and mechanical/chemical stability.

Our on-chip lensless cameras can be practically adapted in various ways to account for the advantages of a recently-emerging class of lensless cameras. A broad range of applications is available with choosing image sensors with different formats. For example, we could indeed implement the same fabrication method in tiny image sensors for subminiature cameras for private use and endoscope cameras for the medical industry. As the thickness of the camera module and image sensor does not correlate in lensless cameras, large-format sensors can be used to make thin camera modules with improved image quality. In addition, since computational image reconstruction in a lensless camera does not require the pixels in the image sensors to be organized in a dense 2D array, more creative arrangements of the cameras can be realized.

Lensless imaging is a new method that continues to improve and expand. Our method and the prototype device currently have limitations that call for more technical improvement in the field. For instance, reconstructed image quality is still low compared to lensed cameras with the same pixel resolution. This is a general issue in lensless imaging, where various approaches

such as optimized design for the phase masks and deep-learning-based reconstruction and image enhancement are currently being developed. Moreover, the 10% optical transmittance loss of PUA 311 with a thickness of  $\sim 1$  mm might affect the image quality. Acquiring bright scenes may be needed to minimize the transmittance issue. We used 3D printed structure to control the thickness of the PUA diffuser, which is acceptable in our prototype. A better fabrication method for sophisticated thickness control is the remaining improvement. Specific to our device, we can further improve the image quality by adding an aperture at the expense of light throughput or using a master phase mask with diffractive elements designed for sharper and sparser PSF patterns. Using deep learning with large training data is also a promising direction. With these future improvements ahead, we expect that the merits of our fabrication method will become more explicit and contribute to the advancement of the field of computational imaging devices.

#### ACKNOWLEDGMENT

The authors would like to thank Kyungwon Lee and Changyoon Yi for their assistance in the experiment.

#### REFERENCES

- [1] M. Z. Chowdhury, M. T. Hossain, M. Shahjalal, M. K. Hasan, and Y. M. Jang, "A new 5G ehealth architecture based on optical camera communication: An overview, prospects, and applications," *IEEE Consum. Electron. Mag.*, vol. 9, no. 6, pp. 23–33, Nov. 2020.
- [2] J. Lim, J. Seo, and Y. Baek, "Camthings: IoT camera with energy-efficient communication by edge computing based on deep learning," in *Proc. 28th Int. Telecommun. Netw. Appl. Conf.*, 2018, pp. 1–6.
- [3] M. Cornacchia, K. Ozcan, Y. Zheng, and S. Velipasalar, "A survey on activity detection and classification using wearable sensors," *IEEE Sensors J.*, vol. 17, no. 2, pp. 386–403, Jan. 2017.
- [4] W. Zhang, Y. Zou, T. Lin, F. S. Chau, and G. Zhou, "Development of miniature camera module integrated with solid tunable lens driven by MEMS-thermal actuator," *J. Microelectromech. Syst.*, vol. 26, no. 1, pp. 84–94, 2017.
- [5] A. Brückner, A. Oberdörster, J. Dunkel, A. Reimann, M. Müller, and F. Wippermann, "Ultra-thin wafer-level camera with 720p resolution using micro-optics," *Proc. SPIE*, vol. 9193, pp. 245–252, 2014. [Online]. Available: <https://doi.org/10.1117/12.2061006>
- [6] H. M. Kim, M. S. Kim, G. J. Lee, H. J. Jang, and Y. M. Song, "Miniaturized 3D depth sensing-based smartphone light field camera," *Sensors*, vol. 20, no. 7, 2020, Art. no. 2129. [Online]. Available: <https://www.mdpi.com/1424-8220/20/7/2129>
- [7] H. L. Phan *et al.*, "Artificial compound eye systems and their application: A review," *Micromachines*, vol. 12, no. 7, 2021, Art. no. 847. [Online]. Available: <https://www.mdpi.com/2072-666X/12/7/847>
- [8] X. Ni, S. Ishii, A. V. Kildishev, and V. M. Shalaev, "Ultra-thin, planar, babinet-inverted plasmonic metalenses," *Light: Sci. Appl.*, vol. 2, no. 4, pp. e72–e72, Apr. 2013. [Online]. Available: <https://doi.org/10.1038/lsa.2013.28>
- [9] V. Boominathan, J. T. Robinson, L. Waller, and A. Veeraraghavan, "Recent advances in lensless imaging," *Optica*, vol. 9, no. 1, pp. 1–16, Jan. 2022. [Online]. Available: <http://www.osapublishing.org/optical/abstract.cfm?URI=optica-9-1-1>
- [10] A. Ozcan and E. McLeod, "Lensless imaging and sensing," *Annu. Rev. Biomed. Eng.*, vol. 18, pp. 77–102, 2016.
- [11] A. Ozcan and U. Demirci, "Ultra wide-field lens-free monitoring of cells on-chip," *Lab Chip*, vol. 8, no. 1, pp. 98–106, 2008.
- [12] M. J. DeWeert and B. P. Farm, "Lensless coded-aperture imaging with separable doubly-toeplitz masks," *Opt. Eng.*, vol. 54, no. 2, 2015, Art. no. 023102.
- [13] G. Kuo, F. L. Liu, I. Grossrubatscher, R. Ng, and L. Waller, "On-chip fluorescence microscopy with a random microlens diffuser," *Opt. Exp.*, vol. 28, no. 6, pp. 8384–8399, 2020.
- [14] J. K. Adams *et al.*, "In vivo fluorescence imaging with a flat, lensless microscope" 2020. [Online]. Available: <https://www.biorxiv.org/content/10.1101/2020.06.04.135236v2.full>
- [15] J. K. Adams *et al.*, "Single-frame 3D fluorescence microscopy with ultraminiature lensless flatscope," *Sci. Adv.*, vol. 3, no. 12, 2017, Art. no. e1701548.
- [16] I. Reshetouski *et al.*, "Lensless imaging with focusing sparse ura masks in long-wave infrared and its application for human detection," in *Proc. 16th Eur. Conf. Comput. Vis.*, Glasgow, U.K.; Cham, Switzerland: Springer, 2020, pp. 237–253.
- [17] F. L. Liu, G. Kuo, N. Antipa, K. Yanny, and L. Waller, "Fourier diffuser-scope: Single-shot 3D Fourier light field microscopy with a diffuser," *Opt. Exp.*, vol. 28, no. 20, pp. 28969–28986, 2020.
- [18] K. Monakhova, K. Yanny, N. Aggarwal, and L. Waller, "Spectral diffuser-cam: Lensless snapshot hyperspectral imaging with a spectral filter array," *Optica*, vol. 7, no. 10, pp. 1298–1307, 2020.
- [19] V. Boominathan, J. K. Adams, J. T. Robinson, and A. Veeraraghavan, "PhlatCam: Designed phase-mask based thin lensless camera," *IEEE Trans. Pattern Anal. Mach. Intell.*, vol. 42, no. 7, pp. 1618–1629, Jul. 2020.
- [20] M. S. Asif, A. Ayremlou, A. Sankaranarayanan, A. Veeraraghavan, and R. G. Baraniuk, "FlatCam: Thin, lensless cameras using coded aperture and computation," *IEEE Trans. Comput. Imag.*, vol. 3, no. 3, pp. 384–397, Sep. 2017.
- [21] S. Jiang *et al.*, "Wide-field, high-resolution lensless on-chip microscopy via near-field blind ptychographic modulation," *Lab Chip*, vol. 20, no. 6, pp. 1058–1065, 2020.
- [22] J. Tan *et al.*, "Face detection and verification using lensless cameras," *IEEE Trans. Comput. Imag.*, vol. 5, no. 2, pp. 180–194, Jun. 2019.
- [23] D. G. Stork and P. R. Gill, "Lensless ultra-miniature CMOS computational imagers and sensors," in *Proc. 7th Int. Conf. Sensor Technol. Appl. Sensorcomm*, 2013, pp. 186–190.
- [24] N. Antipa, P. Oare, E. Bostan, R. Ng, and L. Waller, "Video from stills: Lensless imaging with rolling shutter," in *Proc. IEEE Int. Conf. Comput. Photography*, 2019, pp. 1–8.
- [25] K. Yanny *et al.*, "Miniscope3D: Optimized single-shot miniature 3D fluorescence microscopy," *Light: Sci. Appl.*, vol. 9, no. 1, pp. 1–13, 2020.
- [26] Z. Cai, J. Chen, G. Pedrini, W. Osten, X. Liu, and X. Peng, "Lensless light-field imaging through diffuser encoding," *Light: Sci. Appl.*, vol. 9, no. 1, pp. 1–9, 2020.
- [27] R. Kuschmierz, E. Scharf, D. F. Ortégón-González, T. Glosemeyer, and J. W. Czarske, "Ultra-thin 3D lensless fiber endoscopy using diffractive optical elements and deep neural networks," *Light: Adv. Manuf.*, vol. 2, no. 4, pp. 1–10, 2021.
- [28] N. Antipa *et al.*, "Diffusercam: Lensless single-exposure 3D imaging," *Optica*, vol. 5, no. 1, pp. 1–9, 2018.
- [29] G. D. Savant, S. A. Kupiec, and J. L. Jansson, "Method and apparatus for making optical master surface diffusers suitable for producing large format optical components," U.S. Patent 6,303,276, Oct. 16, 2001.
- [30] K. Murphy, V. Toal, I. Naydenova, and S. Martin, "Holographic beam-shaping diffractive diffusers fabricated by using controlled laser speckle," *Opt. Exp.*, vol. 26, no. 7, pp. 8916–8922, Apr. 2018. [Online]. Available: <http://www.osapublishing.org/oe/abstract.cfm?URI=oe-26-7-8916>
- [31] "RPC photonics," Accessed: Mar. 17, 2022. [Online]. Available: <https://www.rpcphotonics.com/engineered-diffusers-information/>
- [32] S. Boyd *et al.*, "Distributed optimization and statistical learning via the alternating direction method of multipliers," *Found. Trends Mach. Learn.*, vol. 3, no. 1, pp. 1–122, 2011.
- [33] K. Monakhova, J. Yurtsever, G. Kuo, N. Antipa, K. Yanny, and L. Waller, "Learned reconstructions for practical mask-based lensless imaging," *Opt. Exp.*, vol. 27, no. 20, pp. 28075–28090, 2019.
- [34] R. W. Shuai, K. Yanny, K. Monakhova, and L. Waller, "Multiwienermet: Deep learning for fast shift-varying deconvolution," in *Computational Optical Sensing and Imaging*, Washington, DC, USA: Optical Society of America, 2021, Paper CTh5A–5.
- [35] S. S. Khan, V. Sundar, V. Boominathan, A. Veeraraghavan, and K. Mitra, "FlatNet: Towards photorealistic scene reconstruction from lensless measurements," *IEEE Trans. Pattern Anal. Mach. Intell.*, vol. 44, no. 4, pp. 1934–1948, Apr. 2022.
- [36] P. Chen, X. Su, M. Liu, and W. Zhu, "Lensless computational imaging technology using deep convolutional network," *Sensors*, vol. 20, no. 9, 2020, Art. no. 2661.